RF circuit techniques for transition to 5G advanced

Florinel Balteanu [ID]

Skyworks Solutions Inc., Irvine, CA, USA

Abstract

Worldwide adoption of 5G mobile devices has been one of the main driving engines behind semiconductor industry. Since the initial release in 2020, 5G-enabled devices have surpassed the market penetration of 3G/4G smartphones. 5G brings higher data capacity, low latency, and new applications. These are possible due to lower feature nodes such as FinFET 3 nm/5 nm but also due to improvements of the 5G radio frequency (RF) front-end circuitry. This paper presents 5G RF front-end architectures with novel circuits and measurement details which will be part of future 5G advanced and 6G mobile devices and are easier to be controlled using digital circuitry. The paper presents an envelope-controlled power amplifier (PA) principle, along with a novel simplified calibration architecture designed for 5G/5G+ operating under 6 GHz, as well as for frequency range 2 millimeter-wave PAs. An earlier version of this paper was presented at the 2023 53rd European Microwave Conference and was published in the Proceedings [Balteanu F, Thoomu K, Pingale A, Venimadhavan S, Sarkar S, Choi Y, Modi H, Drogi S, Lee J and Agarwal B (2023) Enabling RF circuit techniques for 5G and beyond In *53rd European Microwave Conference (EuMC)*, Berlin, Germany, 22–25].

CAMBRIDGE UNIVERSITY PRESS

Introduction

The continuous need for high data rate (DR) and more mobile applications has been a major driver in rapid adoption of 5G and WiFi7, as well the intense research activity for 6G [1–3]. According to the International Telecommunication Union (ITU), there were more than 8.58 billion mobile subscriptions in use worldwide in 2022, compared to a global population of 7.95 billion (Fig. 1). 5G smartphones uses sub-6 GHz bands and mmWave spectrum [4] together with other RF technologies such as ultra-wideband (UWB), sensing, and computation techniques [5, 6]. 5G will continue to grow fueled by capability to support a variety of new and enhanced services, for example vehicle-to-vehicle (V2X) communications, factory automation, eHealth [7], autonomous vehicle [8], and Internet of things [9]. Today, mobile phones are ubiquitous and for the 650 million smartphones sold worldwide in 2022 more than half are 5G capable. 5G smartphones need to carry over the legacy voice (2G/3G) and need to integrate sub-6 GHz bands known as frequency range 1 (FR1). There is a significant pressure to maintain a balance between the increase functionality and the added cost and size associated with it. As a result, a limited number of 5G stock-keeping units include mmWave modules. There are many advanced developments related to 5G bands, as well the adoption of 6G. It is anticipated that upcoming 5G+ smartphones will incorporate new sensing and interface circuitry to accommodate the new RF bands (Fig. 2) associated with this next generation.

The main goals for 5G new radio are to achieve low latency and DRs of 1 GB. To achieve these DRs, 5G smartphones use 4×4 multiple input multiple output (MIMO) and carrier aggregation (CA) [10]. For a wireless system with k MIMO channels, the capacity is determined by the Shannon's formula as:

$$C = B_w \sum_{k=1}^{k} \log_2(1 + \frac{e_k S_k}{N_x + I_k}) \tag{1}$$

where B_w is channel bandwidth, S_k is the transmit power for the multiplexed level k through MIMO, I_k is in-band interference, e_k is the increase through use of envelope tracking (ET) or average power tracking (APT), and N_x is in band thermal noise. With the introduction of mmWave bands, as well the proposal to introduce new bands for 5G/6G [11], the frequency bands are divided into several frequency ranges (Fig. 2):

- FR1 includes all existing 4G bands and new 5G bands and corresponds to 410 MHz–6 GHz; sub-6 GHz bands. These bands are the backbone of 5G deployment and carry the bulk of data traffic right now.
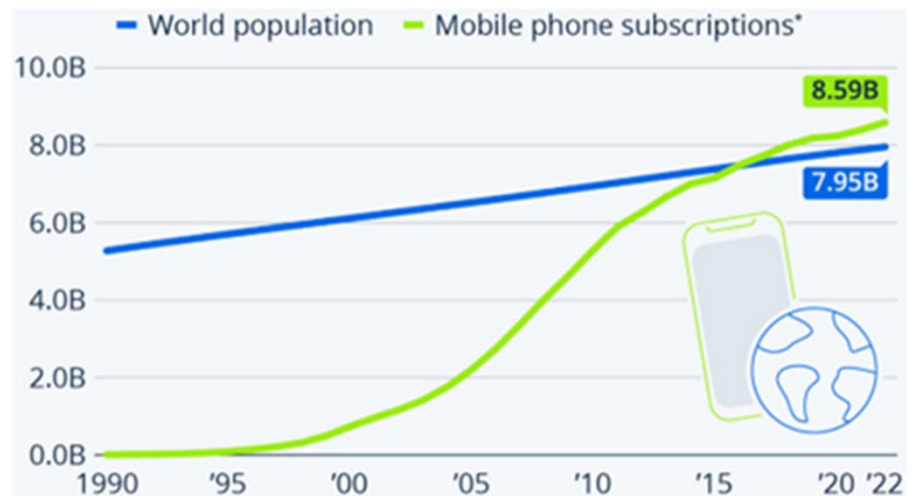
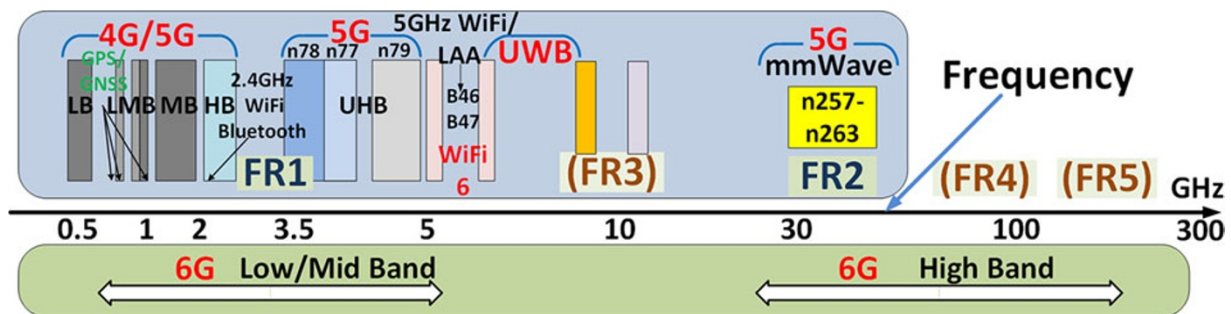**Figure 1.** Smartphone subscription and worldwide population (ITU).

Figure 2. 5G/6G frequency bands.

- Frequency range 2 (FR2) includes new mmWave bands 24.25–71 GHz. Just several smartphones carry mmWave module due to size, power consumption, higher RF propagation loss, and extra cost.
- Frequency range 3 includes bands from 10 to 20 GHz and there are initial discussions in 3rd Generation Partnership Project (3GPP) for future deployment/use for 5G.
- Frequency range 4 covers 52.6–71 GHz and is expected to be used in autonomous vehicles and vehicular radars.
- Frequency range 5 covers 95–325 GHz and will be part of 6G deployment.

Low latency is the prerequisite for real-time applications, such as self-driving and autonomous cars, as well smart machines communicating in real time. Reliable high DR and low latency are important in connecting smart devices in 5G. A typical 5G RF front-end (RFFE) module for 5G mobile devices has six to nine antennas for under 6 GHz space (5G, WiFi, Bluetooth, GPS, and UWB) and 8/16 channels FR2 mmWave module (Fig. 3). Actual smartphones are equipped with multiple antennas that can cover various frequency bands. These antennas are strategically chosen based on the most optimal propagation path to communicate with the base station. To ensure coverage across multiple bands, aperture tuners (ATs) and impedance tuners (ITs) are used to adjust for any mismatch. The selection of the best propagation path is determined by evaluating the maximum signal-to-noise plus interference ratio (SINR).

Cellular RFFE modules and power amplifiers

With the 5G band proliferation there are several RFFE modules in a mobile device covering more than 50 bands. The power amplifier (PA) for RFFE is integrated in the same module (Fig. 4) with several acoustic filters, silicon on insulator (SOI) RF switches, low noise amplifiers (LNAs) for time division duplex (TDD) case, ET circuits, and serial parallel mobile industry processor interface (MIPI RFFE) circuitry [12]. Sub-3 GHz bands provide primary long-term evolution (LTE) cellular coverage and the new 5G bands provide the primary increased capacity using MIMO technology and CA.

One of the most important parts in the RFFE is the PA. With the adoption of 256QAM for 5G uplink (UL) the PA linearity, expressed through error vector magnitude (EVM), is challenging to be achieved (less than 1.85%), although 5G allows 4–5 dB maximum power reduction. Few techniques have been used to meet the efficiency and linearity requirements, the most extensively used and researched being Doherty and ET PAs [13–15]. The adoption of both techniques has been made feasible through advancements in digital signal processing and technology scaling, such as 3 nm/5 nm FinFET. Although Doherty techniques are known for their high efficiency, they do have limitations in terms of broadband operation, back-off mode operation, and handling load mismatch [16–18].

Doherty amplifiers, with n-away structures to increase the bandwidth (BW) (Fig. 5), are currently used in 5G base station [19]. Doherty amplifiers require digital predistortion (DPD) that presents some challenges, especially for higher modulation BW in
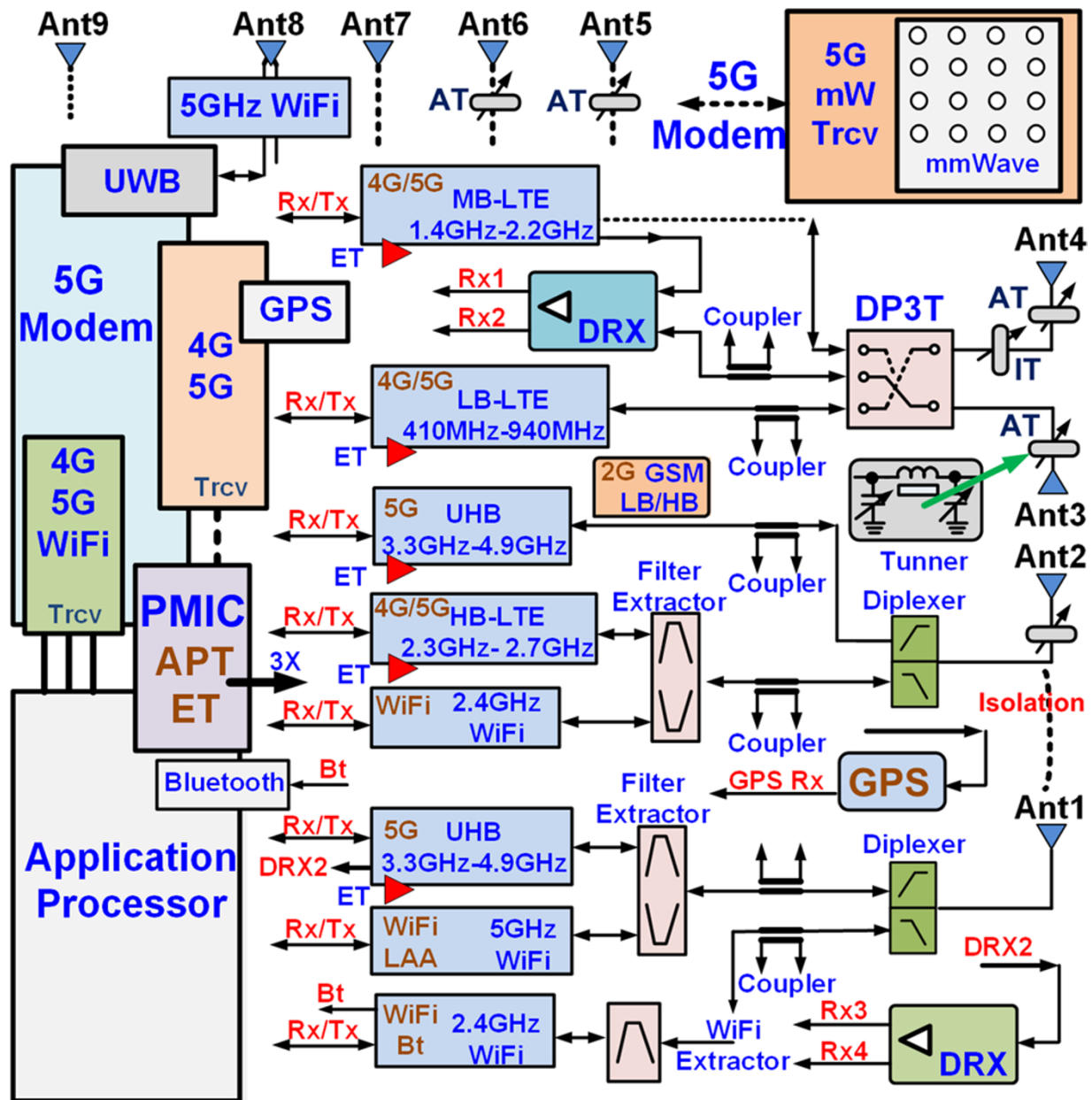
Figure 3. 5G smartphone RF front-end modules architecture.

5G and future 5G+ and 6G. Current 5G systems use DPD but this technique present several challenges:

- With the increase channel BW, e.g., 100 MHz LTE for FR1, the DPD instantaneous BW is 3–5× higher and can be as high as 400–500 MHz. Higher DPD BW is required to reduce the PA memory effects and this requires also high BW for the observation path. Assuming 1 GHz modulation BW for FR2 this task is even more difficult [20–22].
- To get higher DR 5G smartphones use multiband and CA and therefore there is the need for separate DPD processing paths.
- The new 5G FR1/FR2 bands use TDD [23] and one of the main challenges comes from the PA operating on/off in a duty cycle and going through different thermal profiles. DPD must adapt in real time to thermal effects, which may be very challenging for mobile devices.

Actual PAs in mobile devices are broadband class E PAs and are operated most of the time with an ET controller. ET technique was first introduced by Kahn in paper [14] and worked for low signal modulation BW. With the fast development of digital processing and the access to low features such as 3 nm/5 nm/7 nm FinFET and complementary metal oxide semiconductor (CMOS), ET has been deployed in smartphones since 2012. With the introduction of 5G smartphones and the need for a DR of 1 GB [24], there is now a need for multiple PAs to be active simultaneously, hence requiring the use of three ET circuits in certain scenarios. To fully optimize performance and achieve a high modulation BW, the most efficient method is to integrate ET's fast tracker into the RFFE, as shown in Fig. 4. For added convenience, actual well-known smartphones are equipped with three dedicated power management integrated circuits (PMICs) that possess ET capability. These circuits allow for simultaneous control of one to three PAs, as depicted in Fig. 6.
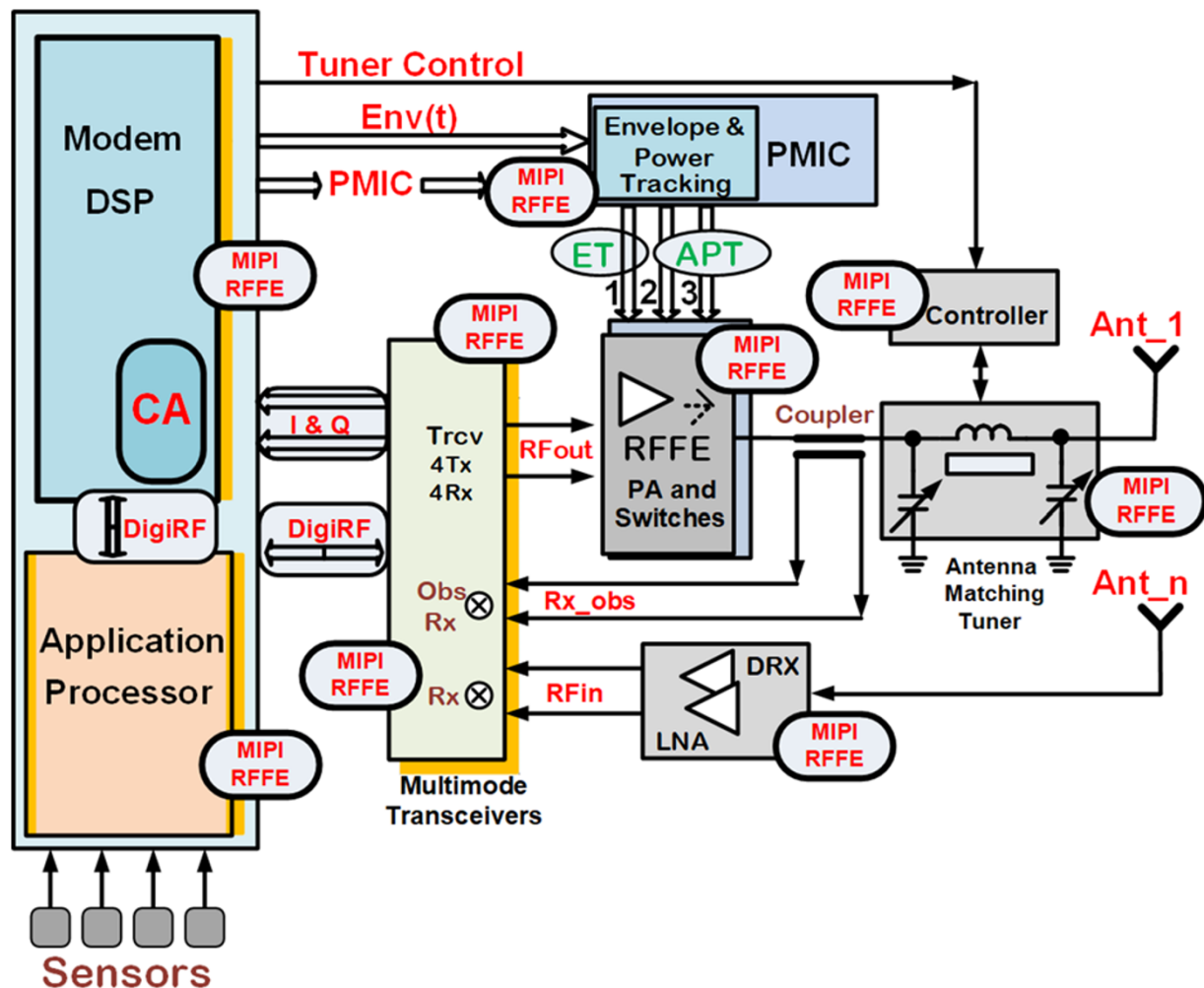
Figure 4. 4G/5G RF front-end module structure.

Figure 5. Three-way Doherty PA.
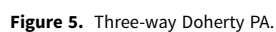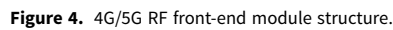
Figure 6. RFFE/ET/PMIC/tuner control schematic.

Due to limitations with modem hardware DPD resources and RF interference, only one PA is currently functioning in ET mode. Two additional PAs are operating in APT mode for CA purpose. The PA, operating in low band (LB) frequency division duplex (FDD) bands, is commonly used as an anchor band. This is due to its lower propagation loss and lowest latency compared with other bands [3, 4, 24].

The modem and application processors drive the advancement of semiconductor technology toward more advanced nodes such as 3 nm/5 nm FinFET, with possibilities of even smaller nodes like 2 nm/FinFET soon. While some smartphones integrate both the modem and application processor on a single die, high-end smartphones often have a separate application processor on a single to allow for customization and enhanced user interface. The modem is responsible for data transfer and communication, with one of its most important tasks being RF communications. With 5G technology, achieving downlink DRs of 1 GB requires multiple 5G RF receivers and transmitters to operate simultaneously. However, practical applications deviate from Shannon theory's assumption (Eq. 1) of an isotropic system without delay. Instead, they require synchronization, delay calibration (such as ET delay calibration), and error correction due to anisotropic nature (Fig. 7) of transmit/receive processes. Delay calibration helps improve signal quality during RF transmission operations while other settings

on the Tx/Rx channels must be programmed accordingly for optimal performance. Actual modems can combine four channels for receiving data at a maximum rate of 3 GB and transmitting data through three channels at a rate of 500 MB. These impressive DRs are typically achieved under laboratory conditions and are much lower in real-world deployment scenarios.

The modem interfaces with peripheral devices, including ET/APT PMICs, RFEEs, antenna tuners, and LNA modules through MIPI RFEE; MIPI RFFE has a maximum speed of 52 MHz. To ensure accurate timing for 5G CA, the latest version of the MIPI RFFE standard [12] features enhanced capabilities such as extended triggers, timed triggers, and mappable triggers.

ET is a hybrid transmit technique that combines features from polar modulation and linear modulation. While polar modulation offers the benefit of lower power consumption, it also requires a higher number of bits and presents challenges with delay calibration [25]. As a result, I & Q linear modulation has emerged as the preferred method for 5G transmitters. The linear PA_{in} signal is generated by the transceiver and is used by the RFFE together with the signal Vtrk(t) generated by the ET as presented in Fig. 8. The ET system incorporates delay calibration for the modem generated envelope signal, using the transceiver to observe RF signals. In current 5G mobile devices, two spaced RF signals are employed, and
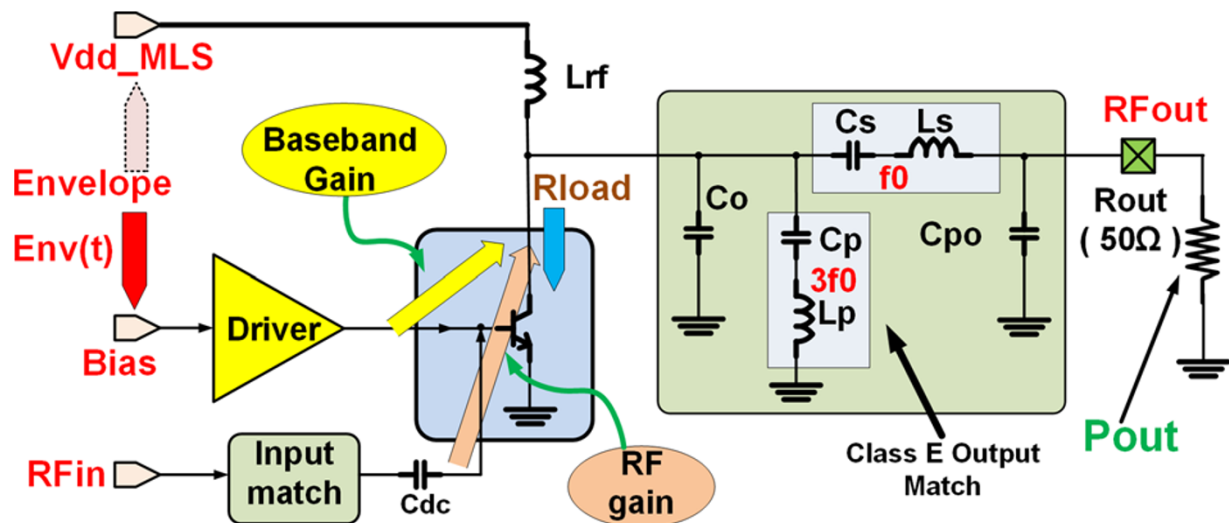
Figure 7. Signal aggregation.

Figure 8. 4G/5G I & Q transmitter diagram.

their peaks are equalized for delay calibration, as outlined in paper [26].

The intermodulation distortion (IMD) introduced by the delay mismatch for a polar system is given by:

$$IMD_{l,r} = 2\pi B_{RF}^2 \Delta_\tau^2 \qquad (2)$$

where B_{RF} is the BW of the RF signal and Δ_τ is the delay mismatch. The Δ_τ minimum between left and right IMD determines the adjacent channel leakage ratio (ACLR) of the ET PA and tracker:

$$ACLR = \min(IMD_{l,r}) + k \qquad (3)$$

where k is a correction factor determined by RF signal peak-to-average power ratio (PAPR) and how much the PA is compressed. 5G NR signals can reach a 10.5 dB PAPR. For linear polar modulation, the driver might be compressed and therefore is very challenging to get the right linearity compared with an ET system using a I & Q modulator, a class E PA, and an envelope signal with a basic look-up shaping table using several points. This solution is simpler

than using a load modulation Doherty PA with phase/gain DPD. As the output power and BW for 5G continue to increase, operating the ET becomes more challenging for modulation BWs exceeding 100 MHz. A new envelope-controlled class E PA structure is proposed and presented in Fig. 9 from this perspective.

The PA maximum output power P_{out}, considering low RF losses in the output match, is given by:

$$P_{out} = k \cdot \frac{(Vdd - Vkn)^2}{R_{load}} \qquad (4)$$

where V_{dd} is the PA voltage supply, V_{kn} is the knee voltage, and R_{load} is the load line. For class E PAs $k = 1.365$ and for class B $k = 0.5$. In ET mode V_{dd} is dynamically modulated with the envelope using an ET PMIC.

To enhance the efficiency of high PAPR 4G/5G transmit (Tx) signals, other techniques have been developed such as dynamic load modulation (DLM), which includes varactor DLM and active load modulation (ALM). ALM utilize active current injection to

Figure 9. Input enveloped-controlled class E power amplifier.
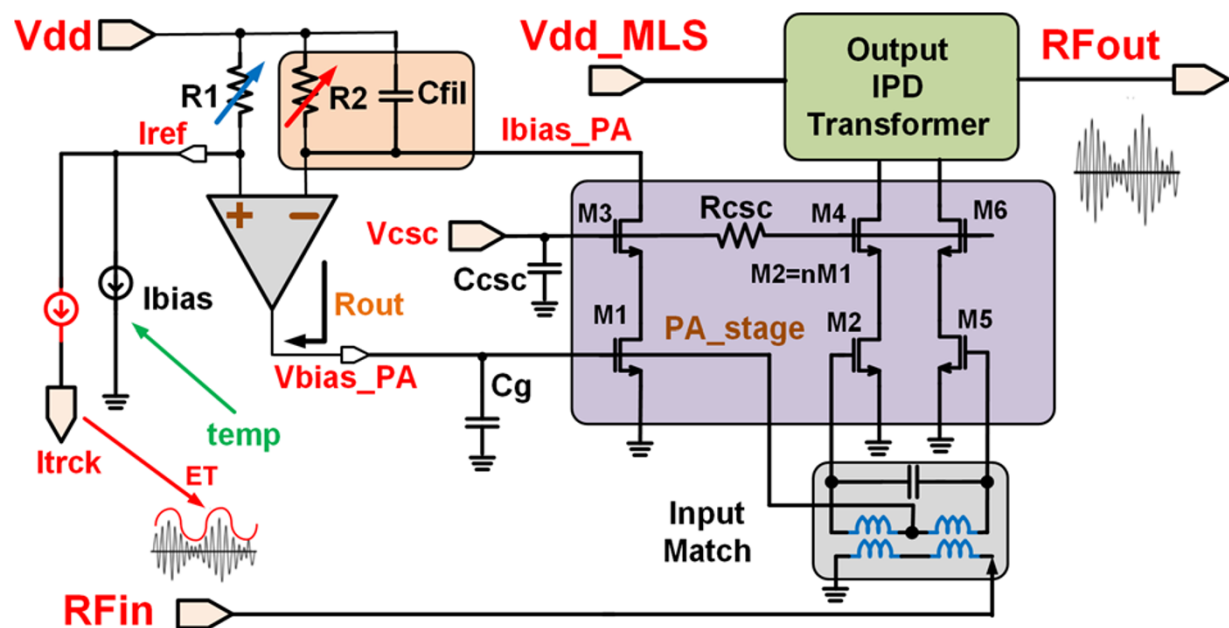

Figure 10. Input enveloped-controlled class E CMOS/SOI differential power amplifier.

tune the load as in Chirex out-phasing PA, Doherty PAs and load modulated balanced amplifier [27]. The PA load line R_{load} is determined mainly by how much current conduction can provide the output transistor. Based on this observation a new envelope-controlled bias PA technique is proposed, as presented in Figs. 9 and 10. The identical envelope signal can be also applied to Vdd line. However, in this scenario, it may require a separate delay calibration or the implementation of multiple level supply control.

The bias driver is connected to the PA core through an RF isolation inductor Lg. The identical schematic concept can be used for a differential PA structure, in such case the input balun provides the required DC isolation (Fig. 10). The servo amplifier used in the bias structure incorporates a current feedback architecture to improve both the frequency response and slew rate, as illustrated in Fig. 11. Vbias_PA supplies the bias for PA, which can be a CMOS or SOI PA

for FR2. The feedback signal Ibias_PA is utilized to sense the output PA current, providing both precise bias and tracking for ET.

Thermal management for RFFE modules

Thermal management of RF power circuits is an essential part of design approach to guarantee RF performances in all operating conditions and avoiding circuits degradation and failure. This becomes even more critical with increased number of PA operating simultaneously, e.g., for 5G there might be three PAs turned on at a time. One of the primary concerns preventing the deployment of SOI technology for PAs in 5G FR1 RFFE is the thermal management. The increase in power delivered to the antenna, reaching up to 26 dBm for high-power user equipment [4, 24] has made this issue even more crucial. A simple schematic for monitoring the
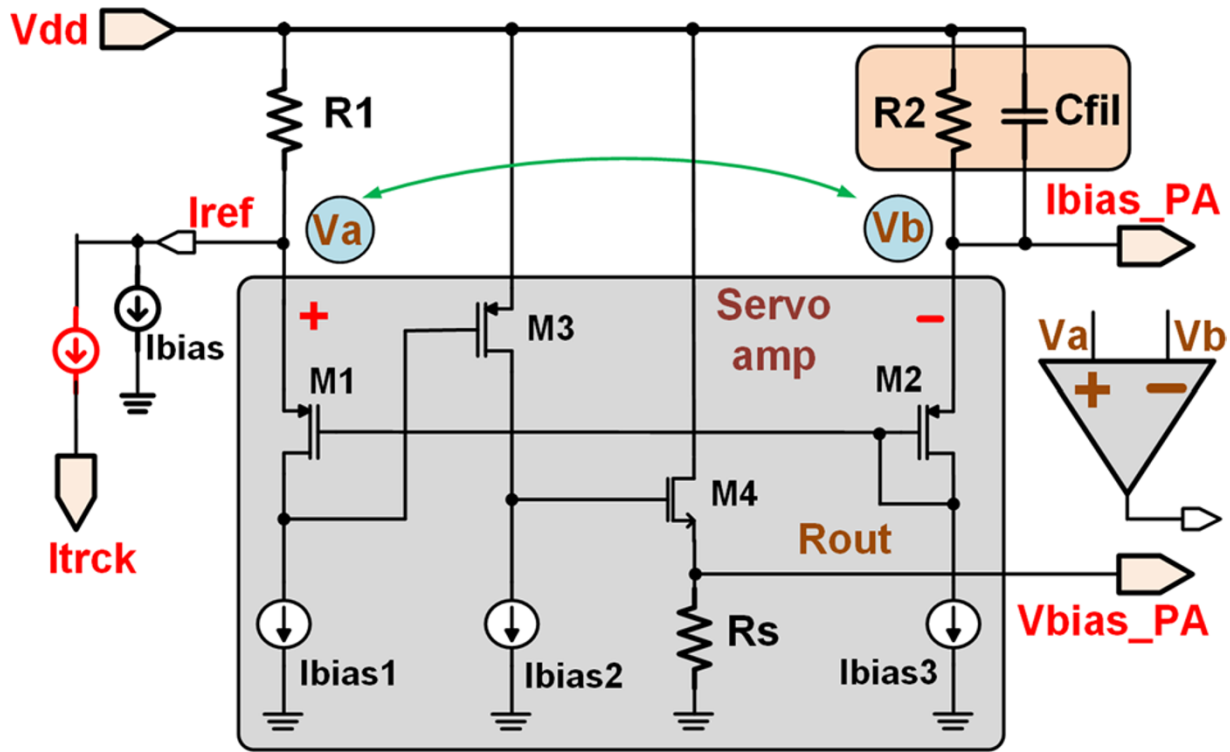
Figure 11. Current feedback servo amplifier structure.

temperature used in current smartphone application is presented in Fig. 12. The analogue value for temperature V_{temp} is used to feed the I_{bias} circuitry and determine the right profile; typically increasing the LNA/PA bias current with the temperature. To obtain an accurate temperature profile, multiple sensors are placed on the CMOS/SOI dies (pn diodes). Additionally, the temperature is digitized and transmitted to the modem via a MIPI RFFE at a speed of maximum 52 MHz. The standard maximum margin of error for this architecture is $\pm 4°C$ at $120°C$. V_{temp} is determined by the equation:

$$Vtemp = Vcal \cdot \left(\frac{Rf}{Rin} + 1\right) - Vd \cdot \frac{Rf}{Rin} \qquad (5)$$

where V_{cal} is the calibration voltage and V_d is the diode voltage. Through calibration all the offsets as well diode voltage variations are cancelled.

The thermal monitor can operate with a fast clock (e.g., 1–5 MHz), as well with a slow clock (25 KHz) to reduce the RF spurs during measurement activity. The thermal monitor can use N elements to map the temperature on a single semiconductor die, especially if there are PAs integrated on the die.

Acoustic filters

The transition from 3G/4G to 5G, with requirements for different RF transmitters coexistence, drives the use of several acoustic filters. For lower frequencies, up to 2 GHz, the filter requirements have been handled using surface acoustic wave (SAW) filters (Fig. 13). With the evolution to 5G and more high and ultra-high bands RFFEs [28], there is a high demand for bulk acoustic wave (BAW) filters and the most used is the film bulk acoustic resonator (FBAR).

To prevent the acoustic waves from dissipating into silicon substrate, an acoustic Bragg reflector is manufactured using thin layer, as seen in solidly mounted resonator BAW. Another approach etches a cavity underneath the active area as in FBAR shown in Fig. 14. Both types of BAW filters have quality factors ranging from 3000 to 4000 (higher than those of SAW filters). However, there are promising results with comparable quality factors for the new lithium tantalate bonded to silicon hybrid substrate silicon SAW [29].

One of the most used 5G band by the cellular operators is the TDD band n41 (2469–2690 MHz), with the FBAR frequency response insertion loss (IL) for this band shown in Fig. 15. In-band ripple of the acoustic filter affects the ET delay calibration. To mitigate in-band ripple, an average delay calibration is required which slows down the calibration time.

The filter has also higher IL at band edges, and this makes difficult to achieve an ACLR lower than −35 dBc (with DPD) at the low side edge of the n41 filter to minimize the emissions in WiFi channels as shown in Fig. 16 for a 5G PA with 100 MHz modulation BW and with an output power of 26 dBm.

Antenna tuners

Current smartphones use several antennas to achieve high DRs through techniques such as CA, MIMO, WiFi with MIMO. Most smartphones are equipped with eight to nine antennas for optimal performance. Utilizing optimal impedance matching and propagation path, the switching between antennas is achieved with high linearity switches to maximize SINR. This is one of several diversity schemes utilized to enhance the quality and dependability of the RF wireless connection to the base station. Each antenna covers several bands, and for these reasons ATs are used together with
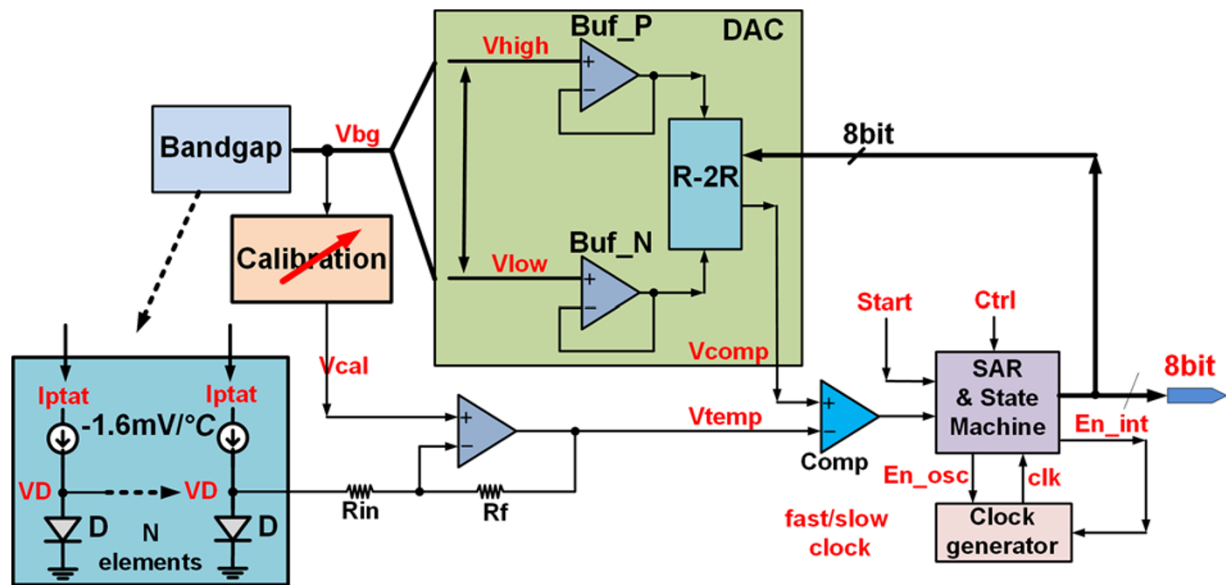
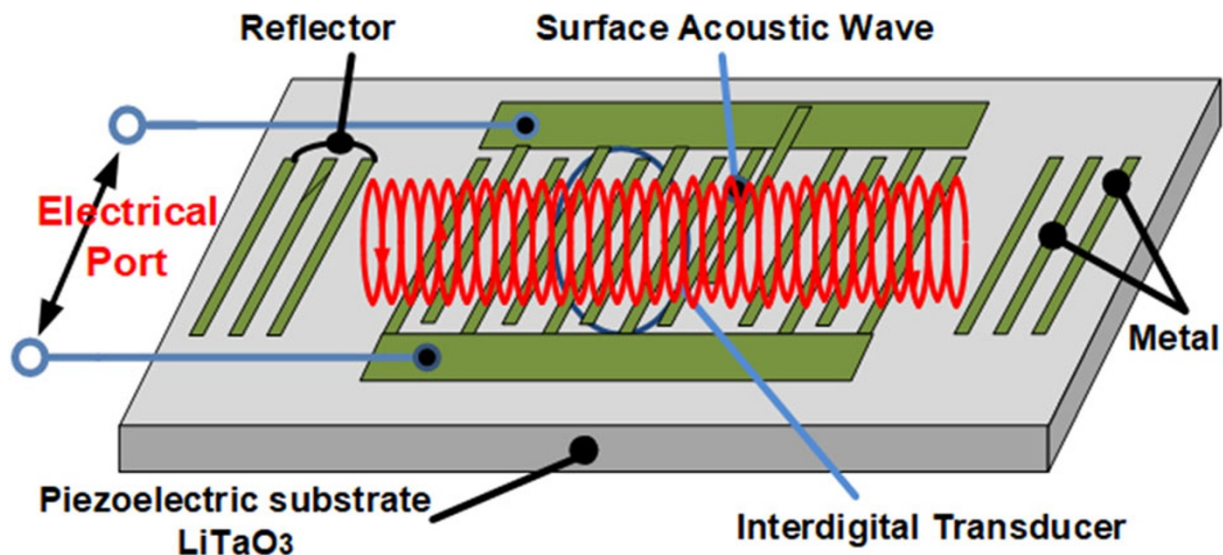**Figure 12.** RFFE thermal monitor circuitry.

Figure 13. SAW filter structure.

ITs to correct the antenna mismatch as presented in Fig. 17. While signals in lower frequency bands have the capability to propagate over long distances and penetrate building with ease, mmWave FR2 signals have a shorter range and do not penetrate solid materials efficiently. Additionally implementing beamforming for mmWave FR2 is more complex than utilizing antenna tuners for bands under 6 GHz [24].

Antenna BW is given by the formula:

$$\frac{df}{f} = k\frac{(a/\lambda)^3}{\eta} \qquad (6)$$

where a is antenna length, λ is the wavelength, η is the antenna radiation efficiency, and f is frequency. From equation (6) covering wider bands can be obtained using larger antennas or lower radiation efficiency which both are undesirable and explain the need

of using antenna tuners. Figure 18 presents the antenna efficiency after tuning for an LB antenna.

To tune the antenna, a coupler is required to be used as shown in Fig. 19 as positioned before the tuner (Cp3). Typically, a coupler has approximatively 0.2 dB RF IL and adds to the power loss. For Cp3 position, the coupler can be used for ET delay calibration [26]. If a full DPD is required to correct the ACLR, the best coupler position is Cp1. While position Cp2 may result in less error in RF power measurement within the band when implementing full DPD, it does not offer as effective ACLR correction.

Implementation and measurements

The gallium arsenide (GaAs) heterojunction bipolar transistor PA, ET driver amplifier together with RF SOI switches and RF FBAR filters are integrated on the same substrate in a multi-chip
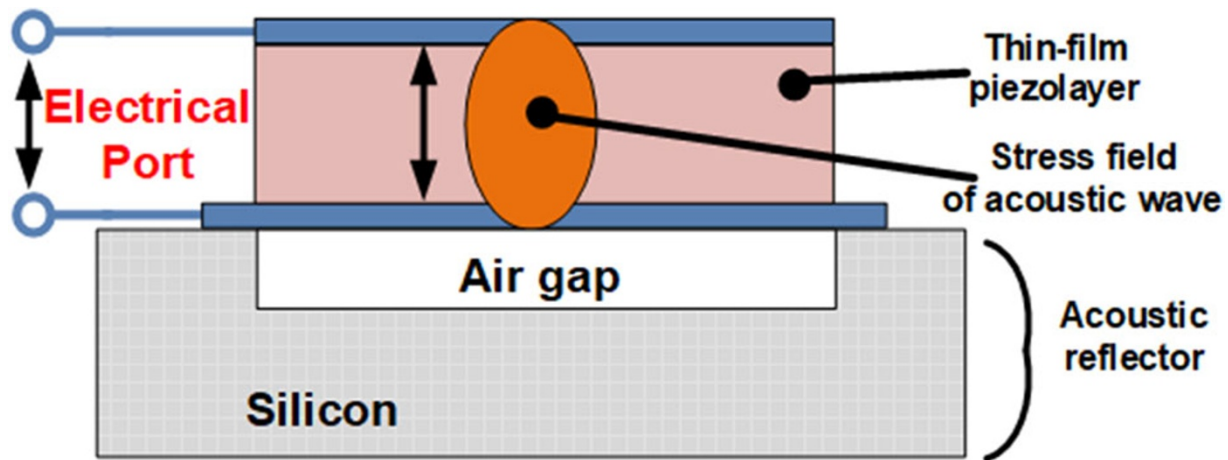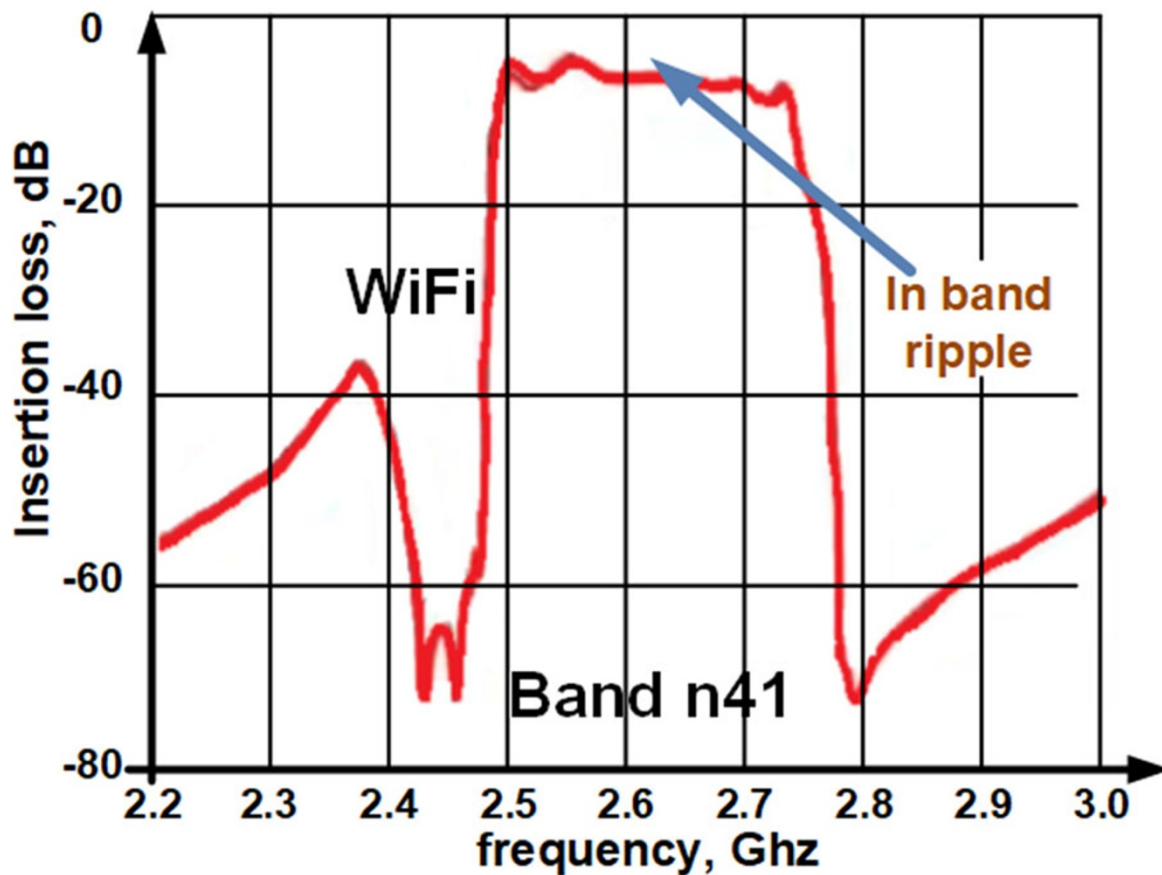
Figure 14. FBAR acoustic filter structure.

Figure 15. FBAR filter response for band n41.

module (MCM). For current FR1 smartphones and 6 GHz RFFE, the ET circuit is connected to the modem via a differential analogue signal Env(t). This interface follows the MIPI ET standard and is known as the eTrack[SM] [12]. Figure 20 presents the interface for the envelope signal Env(t), utilized in the control of a class E PA, based on the proposed concept.

The detailed schematic for transconductor circuit a1 is presented in Fig. 21. Typically, the input voltage levels can reach 1.4 V peak to peak and therefore there is no need of additional gain which will add noise into the ET system. The interface standard has been initially defined to work up to 20 MHz, however it is used currently to operate up to 150 MHz for 5G applications. As the modulation BW increases, a new interface between the modem and ET becomes necessary. This interface must be capable of operating up to 2 GHz. A promising solution is the MIPI-PHY [30] protocol.

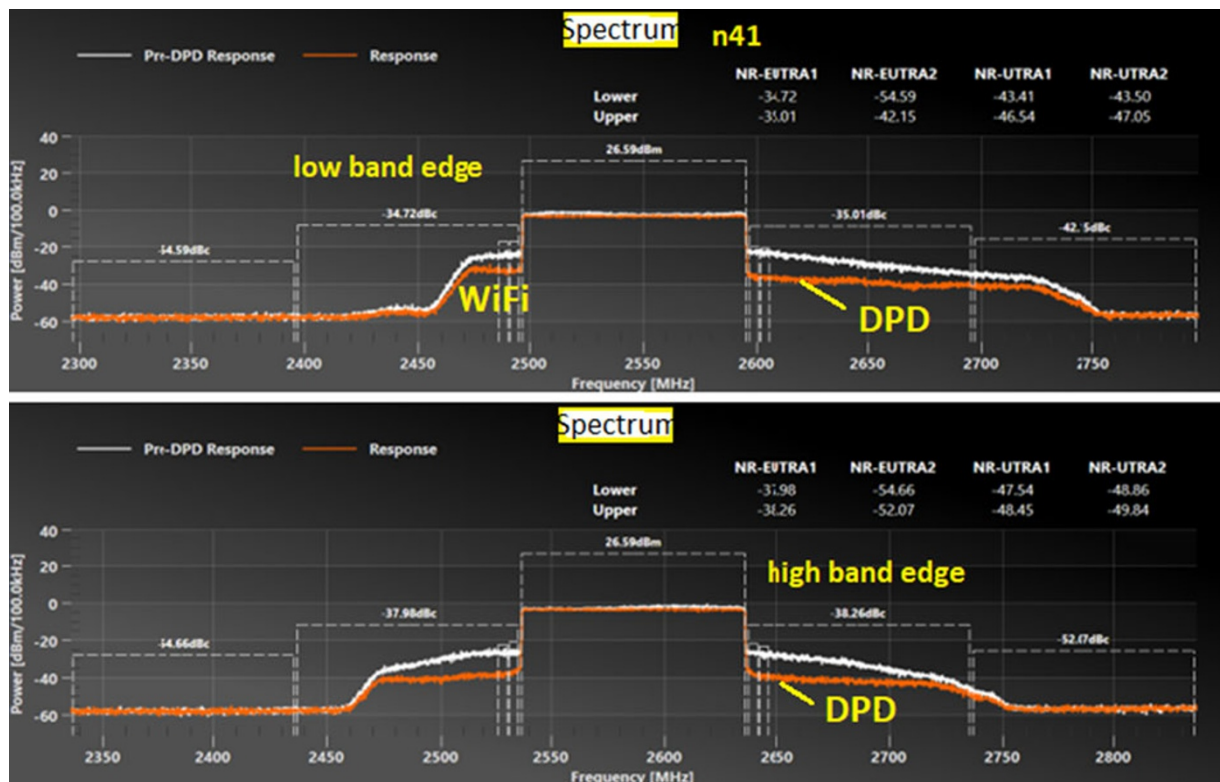The ET signal, Env(t), is a differential signal designed to eliminate common mode noise and prevent interference from

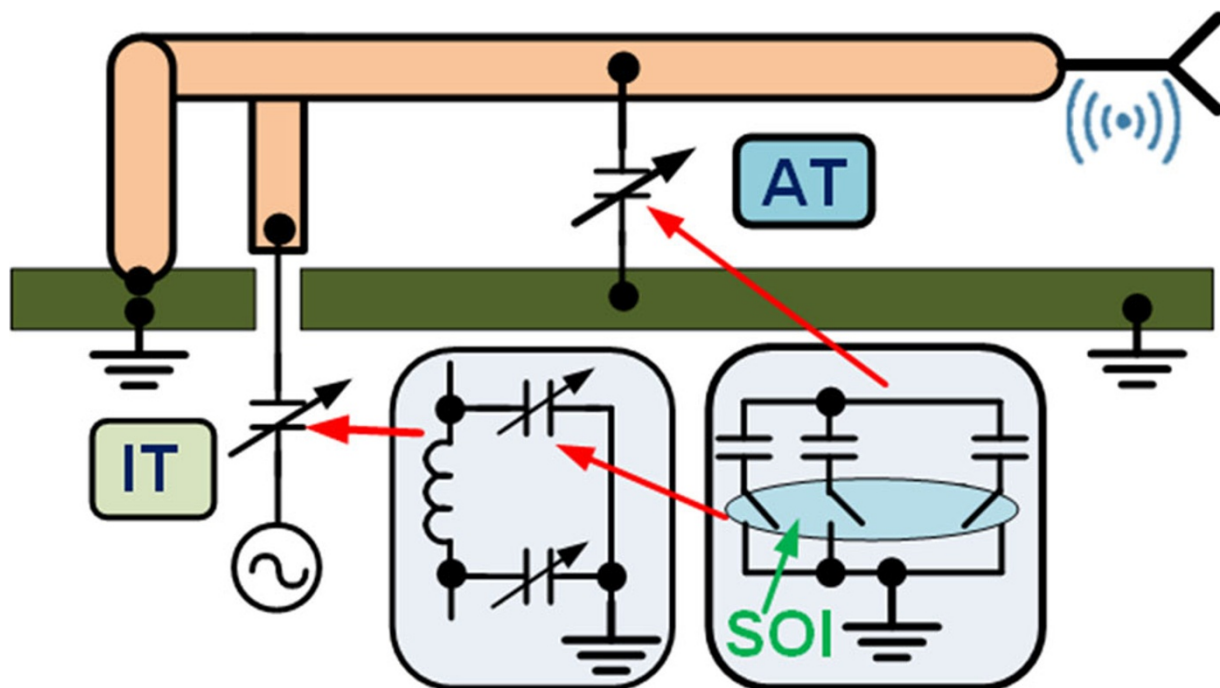**Figure 16.** Band n41 PA and BAW filter under ET operation.

Figure 17. Antenna and impedance tuners.

other signals. Ibias from Fig. 20 sets the desired common mode voltage for the ET interface. The control circuit for the ET presented is implemented using a 0.18 μm CMOS technology and is designed to control a push pull class E GaAs PA, as presented in Fig. 22.

The PA bias current Ibias_PA is determined by the formula:

$$Ibias\_PA = (Itrck + Ibias) \cdot \frac{R1}{R2} \qquad (7)$$

where Itrck is providing the tracking (for ET) and Ibias has a proportional with temperature dependent (PTAT) characteristic
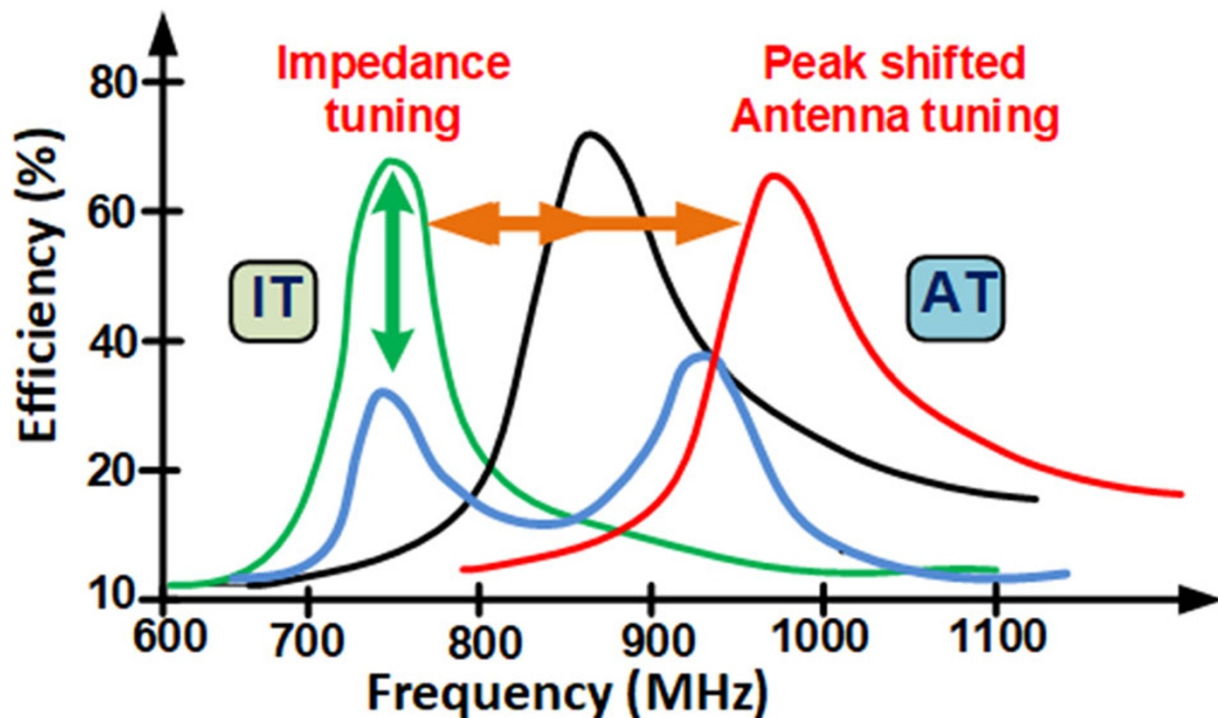
Figure 18. Antenna and impedance tuners response.
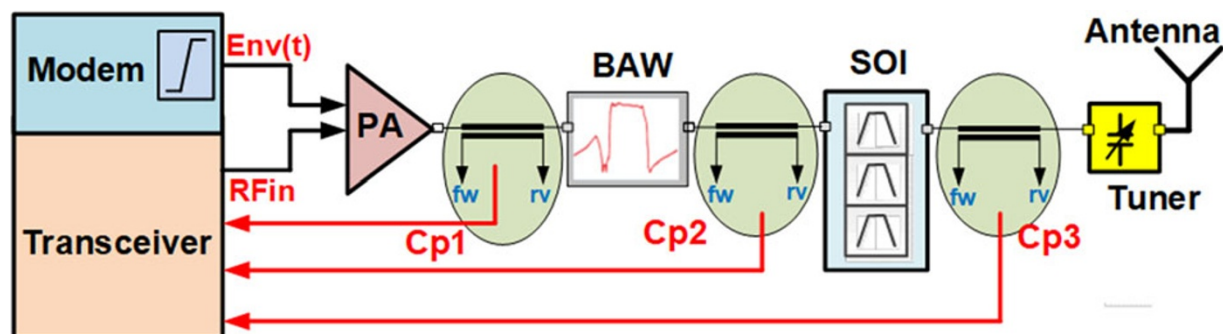

Figure 19. Sub-6 GHZ RFFE coupler positioning.

profile. In FR1 space applications, the ET is only utilized for the final stage, as there are delays in the RF signal between stage 1 and 2 of the PA.

One of challenges in PA control is maintaining consistent behavior of PA across varying temperature, especially in TDD systems. For this reason, Ibias presented in Fig. 10 is proportional with the temperature based on different slopes and the CMOS die sits on GaAs die. This allows for precise temperature sensing of the PA temperature, as depicted for a Mead Band (MB) RFFE in Fig. 23.

For two of 5G bands n41 (FDD Tx 1710–1780 MHz) and n66 (TDD 2496–2290 MHz) the measured performance using an envelope-controlled class E PA is presented in Table 1.

The ACLR is measured using a simple ET look-up table and without DPD; using DPD the ACLR is expected to drop to −45 dBc. For a lower ACLR, without using DPD, the PA added efficiency (PAE) drops to 39% from 42% to 45%, for a minimum gain of 27 dB. As the number of 5G users continues to rise, there is a growing demand for improved 5G network performance. An important metric in evaluating the reliability of a 5G network is the adjacent

channel interference ratio (ACIR), which measures the total leakage between two transmitters. This leakage is determined by both the ACLR and adjacent channel selectivity, as defined by:

$$ACIR = \frac{1}{\frac{1}{ACLR} + \frac{1}{ACS}} \qquad (8)$$

To improve the ACIR, it is necessary to achieve an ACLR higher than −38 dBc, ideally reaching levels as low as −45 dBc using ET and DPD techniques.

The suggested concept of envelope-controlled PA amplifier is applicable for implementation of FR2 mmWave PAs as well. The architecture in Fig. 24 requires a total of three stages to achieve a minimum gain of 26 dB for the Tx PA and Rx LNA in the FR2 5G bands n257–n263.

The ET tracking for FR1 is limited to the last PA stage, while for FR2 it can track the last two stages. Therefore, all bias circuits shown in Fig. 10 are identical to accommodate this implementation as well different modulation BW. One main challenge for FR2
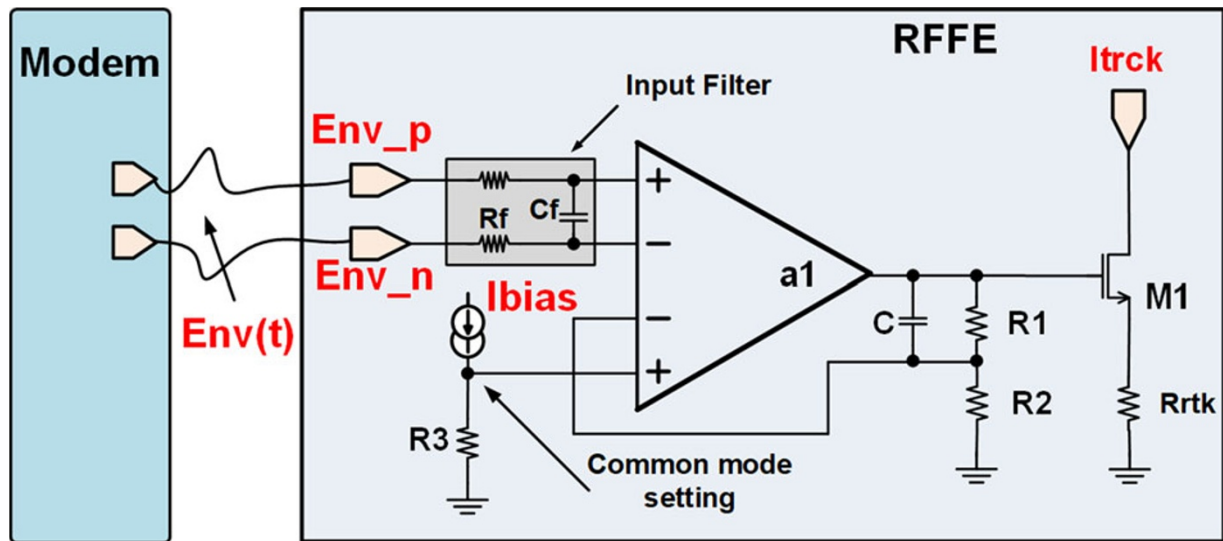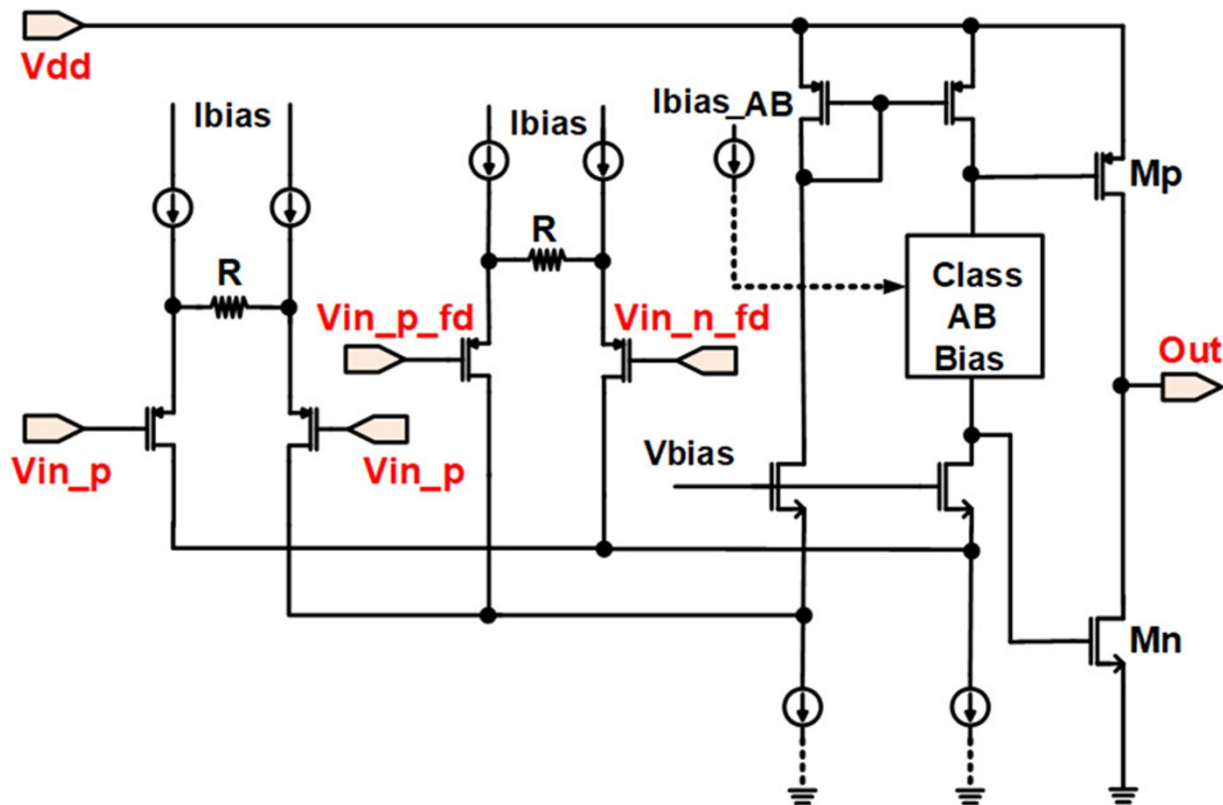
Figure 20. Envelope input circuit.

Figure 21. Envelope input circuit – transconductor detail.

versus FR1 is the calibration procedure involving the bias currents. The RF gain and power are not primarily influenced by the Ibias, in comparison to FR1. The variation in RF gain and power is also affected by a mismatch in local components. Accurate calibration of bias currents for FR2 can be achieved by utilizing precise RF peak detectors to measure and optimize the RF gain.

From this perspective the calibration as well temperature compensation in real time is more complicated as in FR1. Also, for FR2 the modulation BW is increased from 100–150 MHz to 1 GHz.

An FR2 layout amplifier for 5G band n262 (47.2–48.2 GHz) implemented in a 45 nm SOI technology is presented in Fig. 25. The total area for n262 PA is 0.218 mm^2.

The beamforming system utilizes 4/8 integrated PAs on single die. The measured average RF power of one PA operating at 64QAM/200 MHz is 10 dBm, with an EVM of −33.5%. By implementing a basic DPD technique, the EVM improves to a minimum of −36%. One of the limitations for high modulation BW (over 200 MHz) is related to PA thermal behavior. To overcome this, the
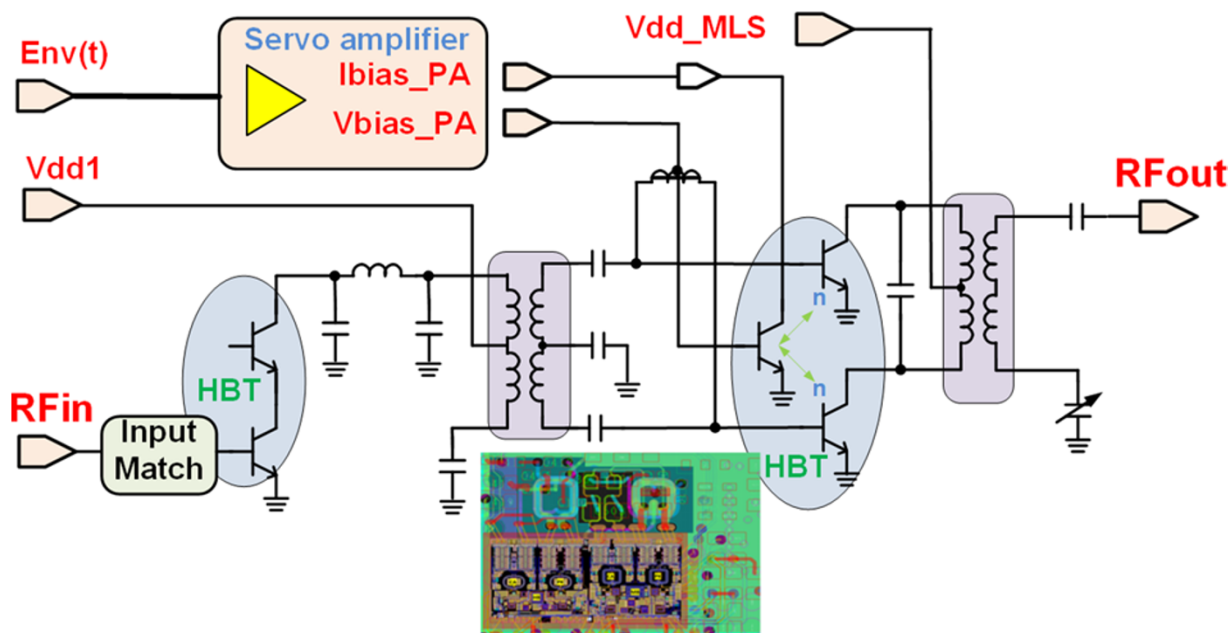
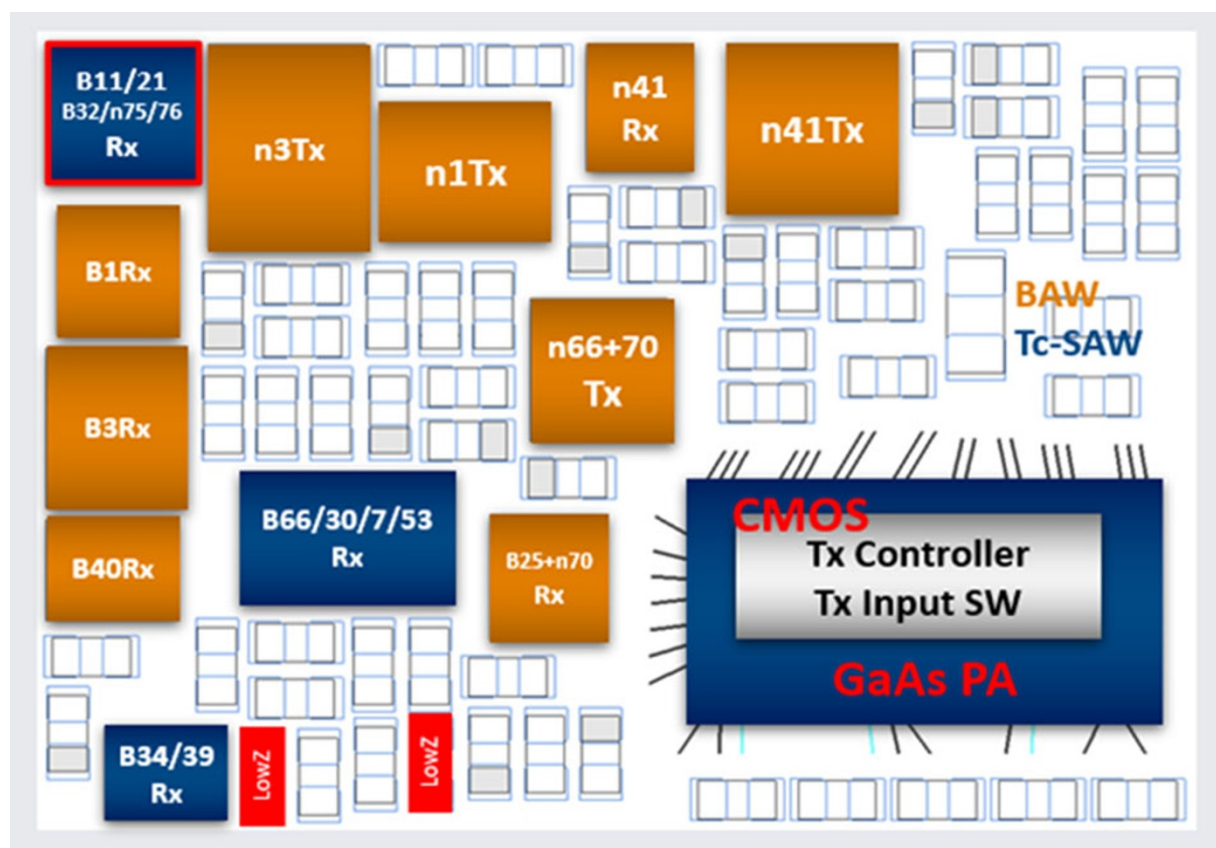**Figure 22.** GaAs push-pull power amplifier.

**Figure 23.** MB RFFE component placement.

implementation uses local temperature detection and compensation circuitry. Utilizing local tracking via bias currents offers a more digital approach to ET for FR2 application, as illustrated in Fig. 26. An envelope-controlled ET approach can use the same look-up table for beamforming. A similar approach with a single look-up table was proposed in paper [21], using Doherty PAs.

For FR2 and high modulation BW the approach of using an observation receiver is not practical and therefore a new method

Table 1. Measurements for 5G bands n66 and n41

Band	Modulation BW	PA_out dBm	PA_out MCM dBm	PAE_out %	PAE MCM %	ACLR dBc
n66	40 MHz	30	26	42	19	−39
n41	100 MHz	32.7	28	45	18	−38
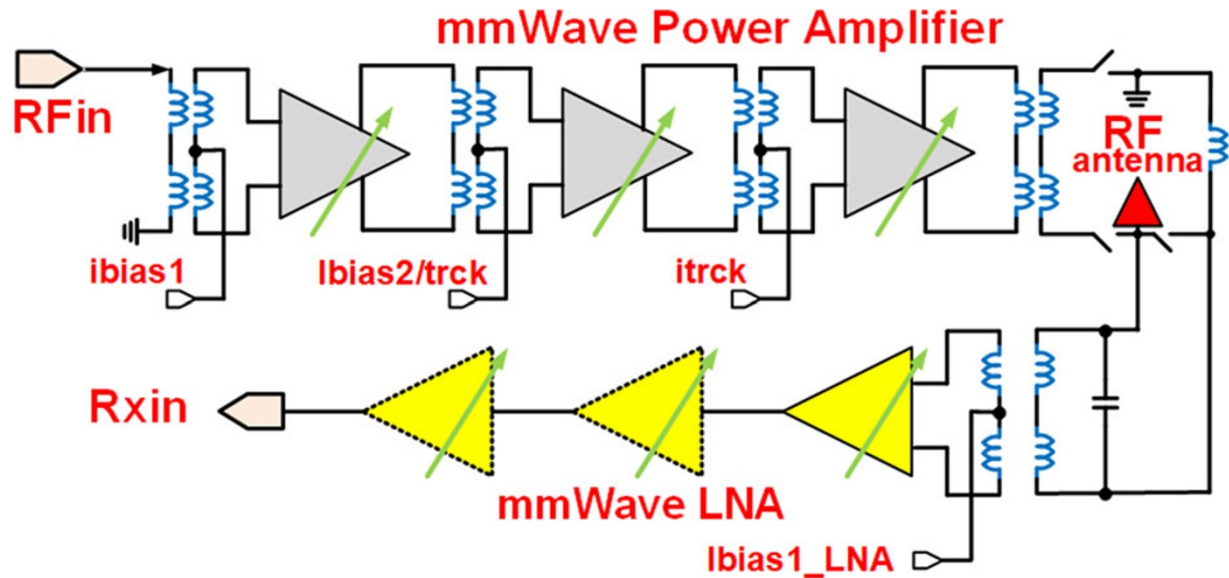
Figure 24. 5G FR2 PA/LNA schematic.
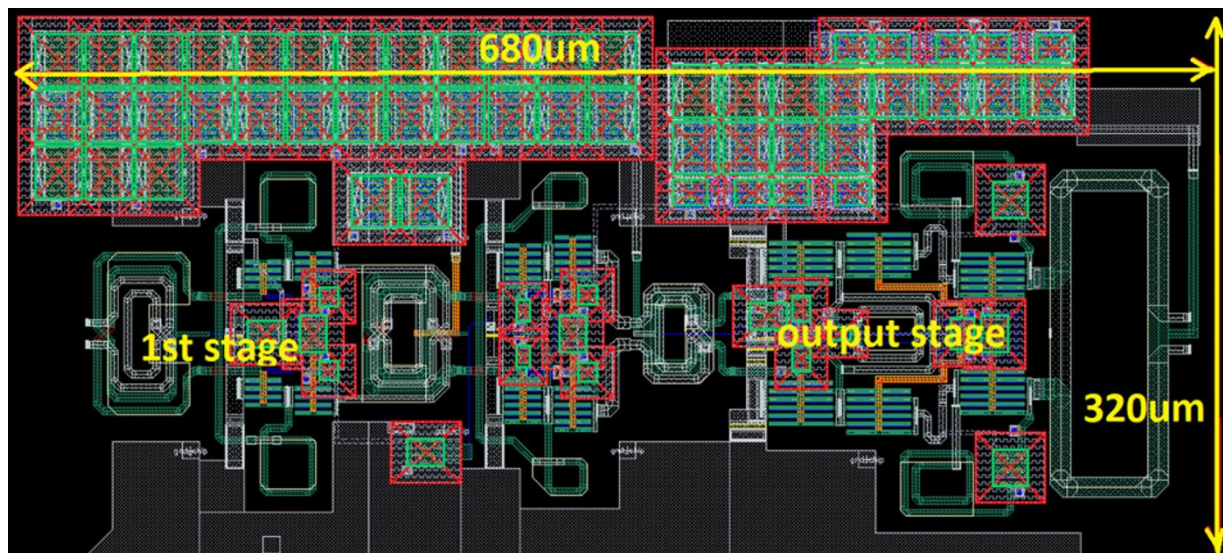
Figure 25. 5G FR2 band n262 layout.

of using precise RF detectors is proposed. The peak/rms detector (Fig. 27) is integrated on the same SOI/CMOS die and connected through a coupler to the PA output. M2 provides the bias, while M1a and RF filter Rd and Cf perform the detection. Similarly, M1b and Rd generate a replica bias with a comparable DC voltage to that of M1a and Rd. The source followers M3 and M4 isolate the RF detection and serve as the interface for the postprocessing circuitry.

The FR2 SOI die uses several RF peak/rms detectors across the die, and they use a single analogue postprocessing circuitry, which interfaces with the transceiver/modem, as shown in Fig. 28. Vcal pin is utilized for calibration of the RF detectors in absence of RF signal.

The measured RF detector shows a precision of 0.1 dB with less than 0.01 dB flatness in band which is more than enough to accommodate the FBAR ripple for TDD band n41 (2.469–2.690 GHz) when the RF detector is used as RF calibration sensor. The RF detector retains its high precision across process variation for FR2 frequencies, as presented in Fig. 29 for band n262.
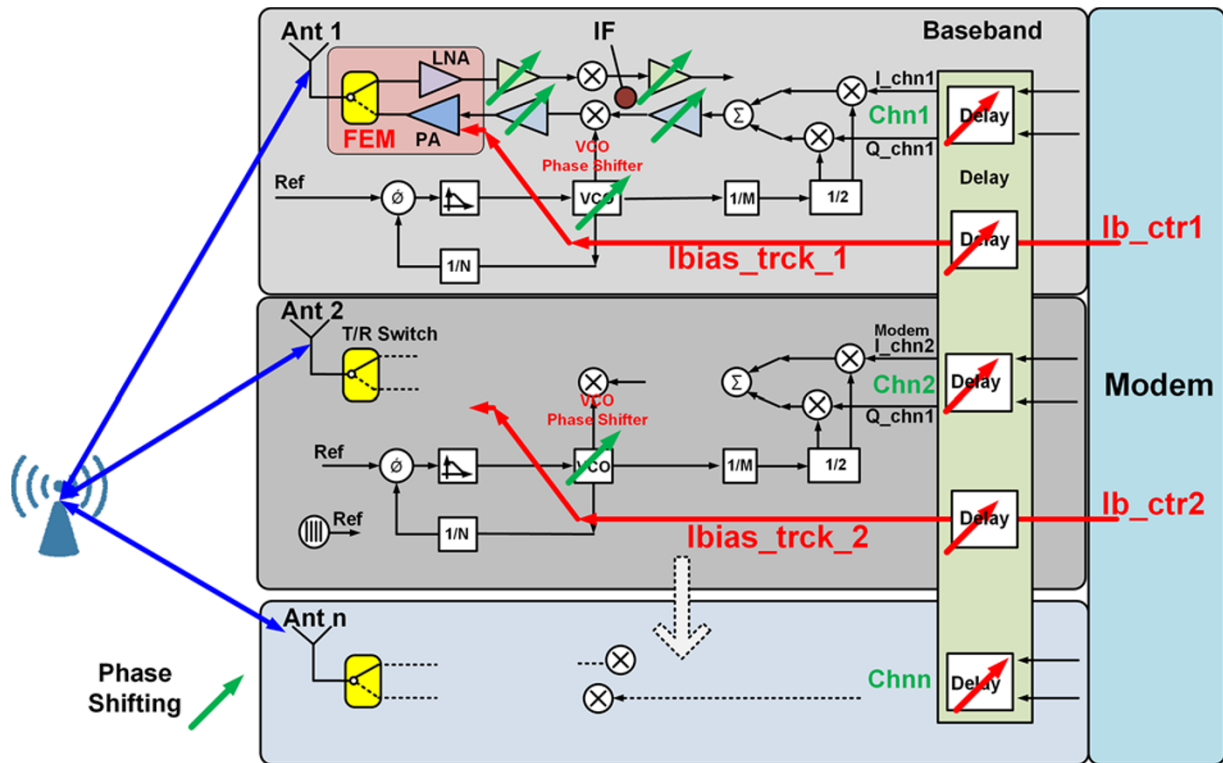
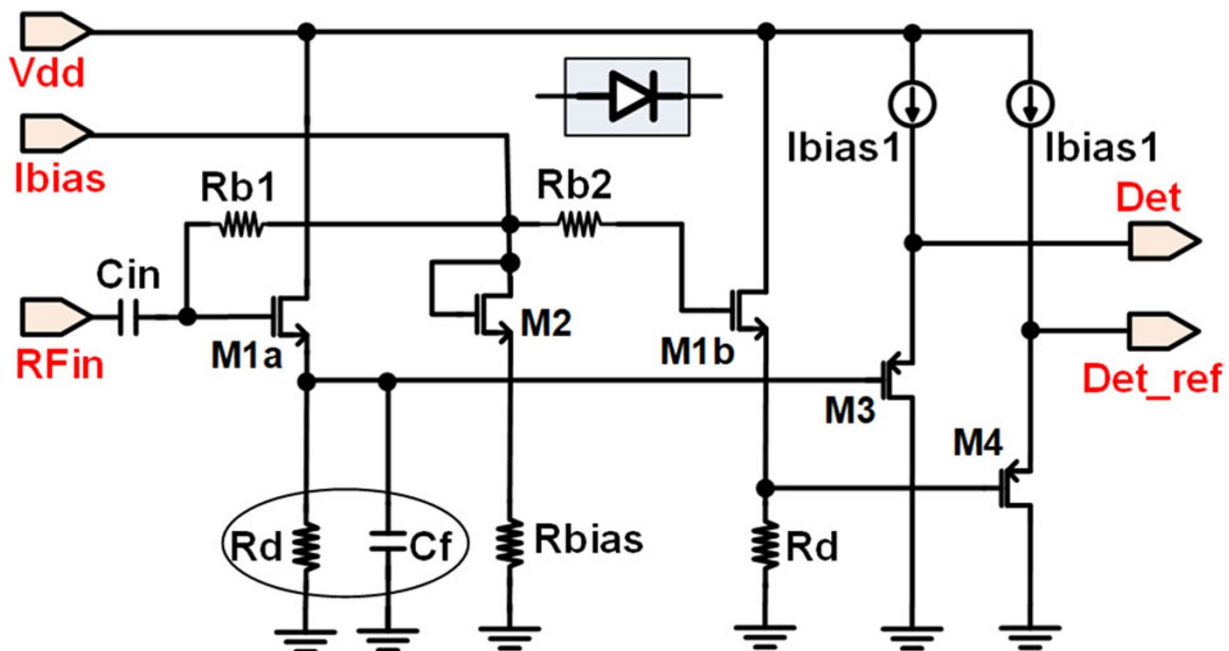**Figure 26.** 5G FR2 beam forming and I_{bias} with ET control.

Figure 27. 5G FR1/FR2 power detector.

Furthermore, the RF detector has a broadband response and the measured time response for 5G FR2 band n262 (48 GHz) is less than 100 ns, as presented in Fig. 30. If the modulation BW for 5G signal is higher (such as 1–2 GHz), the time response can be adjusted through post-detection low-pass RC filters.

The implementation of a fast and accurate RF peak/rms detector for ET and power calibration (Fig. 31) simplifies the calibration structure and takes advantage of the progress in semiconductor technologies, particularly in small feature size, for modern 3 nm/5 nm FinFET technologies. This approach is more straightforward when compared to the current ET calibration of smartphones [31], which utilize observation receivers. The calibration process involves utilizing a slow modulating RF waveform with two RF peak signals, where calibration is achieved when RF detectors
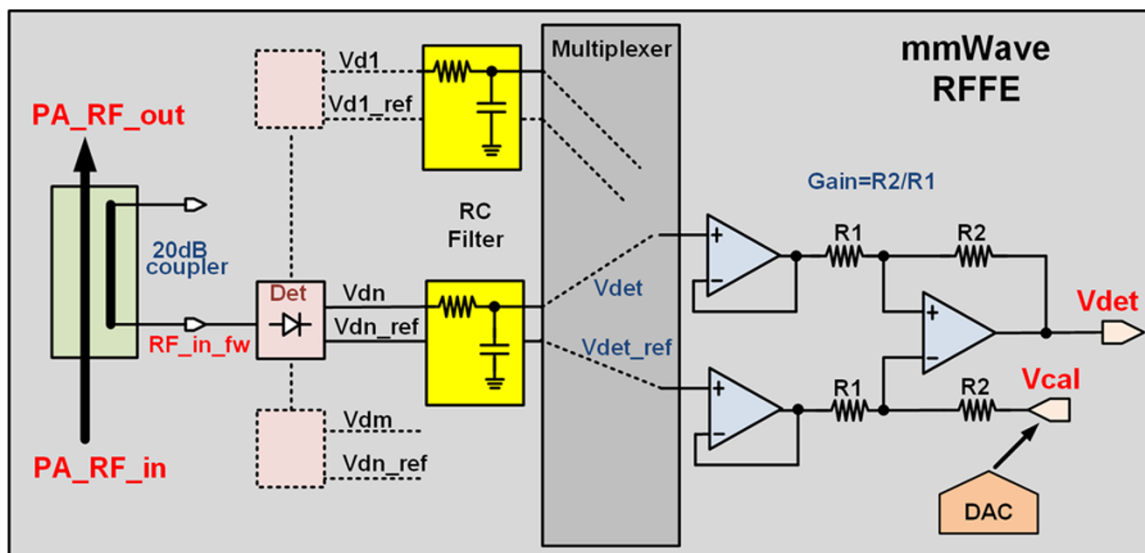
Figure 28. 5G FR1/FR2 power detector analogue postprocessing circuitry.
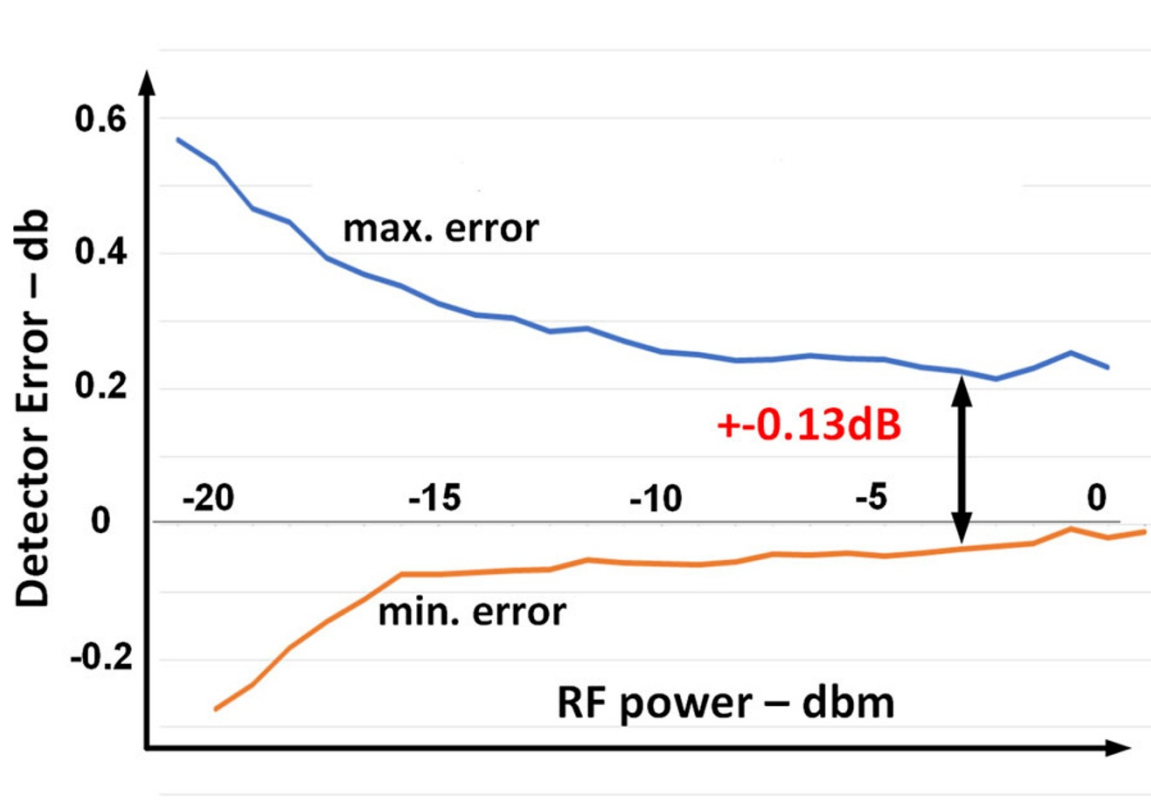

Figure 29. 5G FR2 band n262 power detector error under process variation.

detects equal values for both peaks. The principle closely resembles that of [26] but eliminates the use of impractical observation receivers at FR2 frequencies.

Conclusions

The smartphone industry is a very large and constantly evolving market, where changes in hardware and architecture must undergo extensive validation before being implemented. Despite the introduction of new mobile device models every year, this process takes a significant amount of time. The recent shift from 4G to 5G technology was relatively swift, but it is anticipated that the next major transition to 6G will take longer before full deployment. As such, it is crucial for the cellular industry to diversify its applications and learn from the challenges faced during slow deployment of 5G FR2.
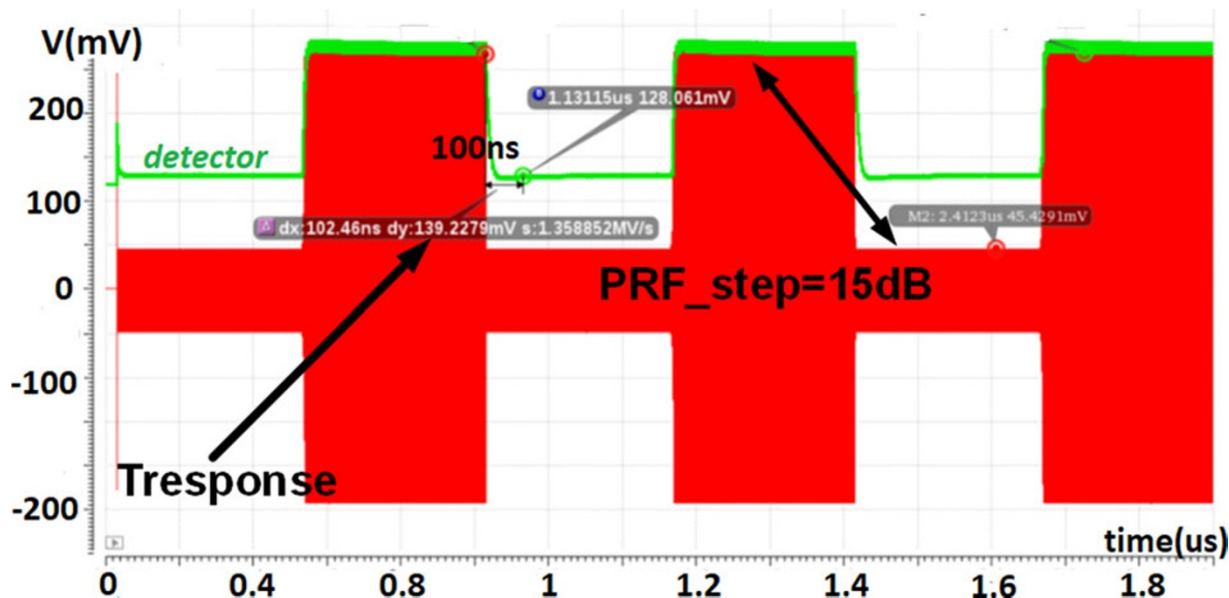
Figure 30. 5G FR2 band n262 power detector time response for CW RF signals.
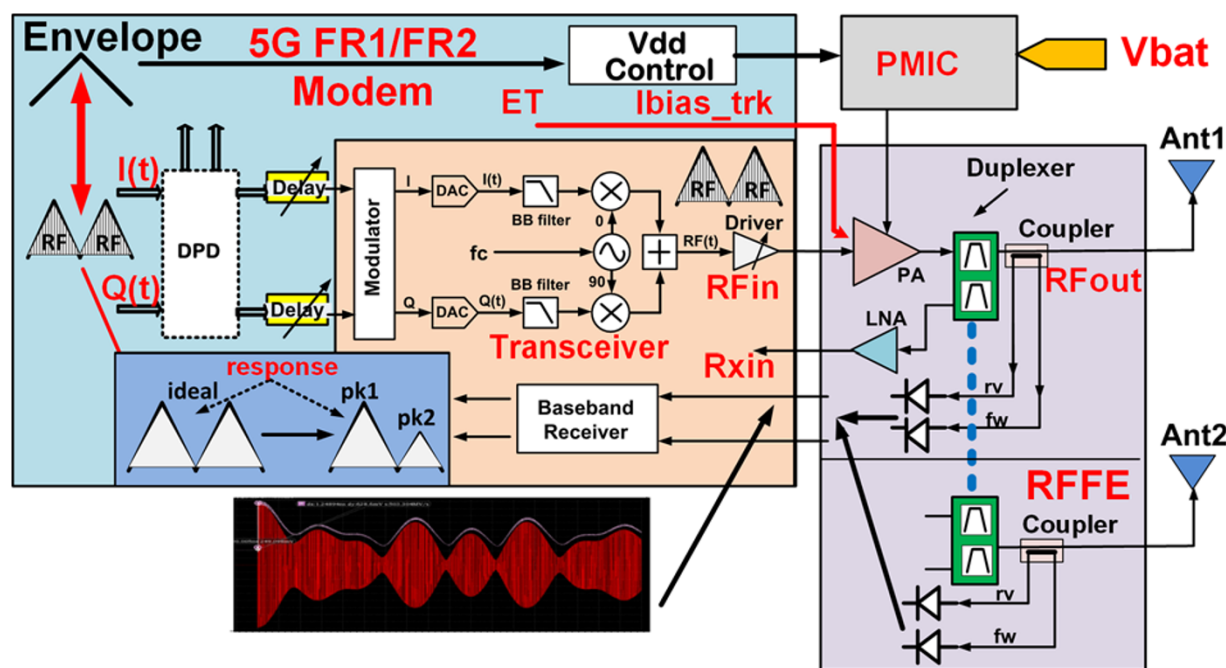

**Figure 31.** 5G ET and power calibration schematic architecture.

To address some of these issues, this paper proposes a RF PA architecture utilizing an envelope-controlled PA and RF ET, as well as precise RF detectors for transmit power calibration. This design has the capability to handle a modulation BW of 2 GHz and support FR2 frequencies. These circuits are currently used for low modulation BW applications on existing mobile devices, but they also pave the way for seamless integration into future generation of RF technologies such as 5G+ and 6G, along with other mobile transmitters.

Competing interests. The author declares none.

References

1. **Balteanu F, Thoomu K, Pingale A, Venimadhavan S, Sarkar S, Choi Y, Modi H, Drogi S, lee J and Agarwal B** (2023) Enabling RF circuit techniques for 5G and beyond. In *53rd European Microwave Conference (EuMC)*, Berlin, Germany, 22–25.
2. **Nakamura T** (2020) 5G evolution and 6G. In *2020 IEEE Symposium on VLSI Technology*, 1–5.
3. **Chen W, Gaal P, Montojo J and Zisimopoulos H** (2021) *Fundamentals of 5G Communications: Connectivity for Enhanced Mobile Broadband and Beyond*. New York: McGraw Hill.
4. **Pehlke D, Brunel D, Walsh K and Kovacic S** (2017) Sub-6GHz 5G for UE, optimizing cell edge user experience. In *IWPC 4G/5G Multi-band, Multi-Mode User Equipment*, Austin, October 2017.

5. **Giordano M, Polese M, Roy A, Castor F and Zorzi M** (2019) A tutorial on beam management for 3GPP NR at mmWave frequency. *IEEE Communications Surveys and Tutorials* **21**(1), 173–196.

6. **Dotlic I, Connell A, Ma H, Clancy J and McLaughlin M** (2017) Angle of arrival estimation using Decawave DW1000 integrated circuits. In *14th Positioning Navigation and Communications (WPNC) Workshop*, 1–6.

7. **Gharba M, Xiao X, Cao H, Eichinger J, Hecker A, Kranzfelder M and Ostler D** (2021) A field test of 5G enhanced mobile ultrasound with network slicing. In *2021 IEEE Globecom Workshops*, Madrid, Spain, 1–6.

8. **Barbi M, Antón RA, Mrozowski HA, Inca S and Monserrat JF** (2022) Simulation-based digital twin for 5G connected automated and autonomous vehicles. In *2022 Joint European Conference on Networks and Communications & 6G Summit (EuCNC/6G Summit)*, Grenoble, France, 273–278.

9. **Al-Fuqaha A, Guizani M, Mohammadi M, Aledhari M and Ayyash M** (2015) Internet of things; A survey on enabling technologies, and applications. *IEEE Communications Survey & Tutorials* **17**(4), 2347–2376.

10. **Balteanu F, Drogi S, Choi Y, Lee J, Modi H, Khesbak S and Agarwal B** (2022) Multiple transmitter coexistence for 5G RF front end modules. In *2021 51st European Microwave Conference (EuMC)*, London, United Kingdom, 180–183.

11. **NTT Docomo Inc.** (2020) White paper "*5G Evolution and 6G*", Tokyo.

12. **Balteanu F** (2022) MIPI RFFE for 5G front end modules. *MIPI DevCon 2022.* https://www.youtube.com/watch?v=if66OOswm3g.

13. **Doherty WH** (1936) A new high efficiency power amplifier for modulated waves. *Proceedings of the Institute of Radio Engineers* **24**(9), 1163–1182.

14. **Kahn R** (1952) Single-sideband transmission by envelope elimination and restoration. *Proceedings of the Institute of Radio Engineers* **40**(7), 803–806.

15. **Grebennikov A** (2019) *Radio Frequency and Microwave Power Amplifiers*. London: IET The Institution of Engineering and Technology.

16. **Zenteno E, Isaksson M and Händel P** (2015) Output impedance mismatch effects on the linearity performance of digitally predistorted power amplifiers. *IEEE Transactions on Microwave Theory & Techniques* **63**(2), 754–765.

17. **Guo J, He S, Shi W, Li C and Zhang X** (2023) A wideband dual-input reconfigurable Doherty power amplifier for mismatch recovery. In *2023 53rd European Microwave Conference (EuMC)*, Berlin, Germany, 271–274.

18. **Singh GD, Mul D, Nemati HM, Alavi MS MS and Vreede LCN** (2022) A load insensitive Doherty power amplifier with better than −39dBc ACLR on 2:1 VSWR circle using a constant 50 Ω trained pre-distorted signal. In *2022 52nd European Microwave Conference (EuMC)*, Milan, Italy, 222–225.

19. **Wong J, Watanabe N and Grebennikov AV** (2018) High-power high-efficiency GaN HEMT Doherty amplifiers for base station applications. In *IEEE Topical Conference on RF/Microwave Power Amplifiers for Radio and Wireless Applications (PAWR)*, 26–41.

20. **Li Z, Pang J, Zhang Y, Yamazaki Y, Wang Q, Luo P, Chen W, Liao Y, Tang M, Wang Y, Fu X, You D, Oshima N, Hori S, Park J, Kunihiro K, Shirane A and Okada K** (2023) A 39-GHz CMOS bidirectional Doherty phased-array beamformer using shared-LUT DPD with inter-element mismatch compensation technique for 5G base station. *IEEE Journal of Solid-State Circuits* **58**(4), 901–991.

21. **Okada K** (2022) Maximizing energy efficiency in sub-THz radio communication and prospective toward 6G. In *2022 IEEE BiCMOS and Compound Semiconductor Integrated Circuits and Technology Symposium (BCICTS)*, Phoenix, AZ, USA.

22. **Wang H, Asbeck PM and Fager C** (2021) Millimetre-wave power amplifier integrated circuits for high dynamic range signals. *IEEE Journal of Microwaves* **1**(1), 299–316.

23. **Pehlke D** (2020) TDD in US and emerging requirements and capabilities for NR, *IWPC 5G User Equipment Evolution*, September 2020.

24. **Balteanu F** (2023) Circuits for 5G front-end modules. *International Journal of Microwave and Wireless Technologies, Cambridge* **15**(6), 909–924.

25. **Madoglio P, Palaskas Y, Angel J, Tomasik J, Hampel S, Schubert P, Preyler P, Mayer T, Bauernfeind T, Plechinger P, Ravi A, Degani O, Banin R, Gordon E, Martev D, Gossmann T, Holm A and Boos Z** (2020) A cellular multiband DTC-based digital polar transmitter with −153-dBc/Hz noise in 14-nm FinFET. *IEEE Journal of Solid-State Circuits* **55**(7), 1830–1841.

26. **Balteanu F, Zhu Y and DiCarlo P** (2021) Envelope alignment calibration in radio frequency systems, *US patent* 11,165,514.

27. **Pednekar PH, Hallberg W, Fager C and Barton TW** (2018) Analysis and design of a Doherty-like RF-input load modulated balanced amplifier. *IEEE Transactions on Microwave Theory & Techniques* **66**(12), 5322–5335.

28. **Balteanu F, Modi H, Choi Y, Lee J, Drogi S and Khesbak S** (2019) 5G RF front end module architectures for mobile applications. In *2019 49th European Microwave Conference (EuMC)*, Paris, France, 252–255.

29. **Ruby R, Gilbert S, Lee SK, Nilchi J and Kim SW** (2021) Novel temperature-compensated, silicon SAW design for filter integration. *IEEE Microwave and Wireless Components Letters* **31**(6), 674–677.

30. **Lancheres P and Hafed M** (2019) The MIPI C-PHY standard: A generalized multiconductor signaling scheme. *IEEE Solid-State Circuits Magazine* **11**(2), 69–77.

31. **Balteanu F, Pingale A, Thoomu K and Choi Y** (2023) Power detection in radio frequency systems, *US patent application* 18/332196.
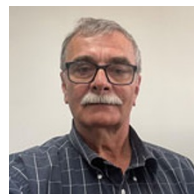
Florinel Balteanu received the M.S. degree in electrical engineering from Polytechnic Institute, Bucharest, Romania, in 1983, and the Ph.D. degree in electrical engineering from Transylvania University, Brasov, Romania, in 1995. From 1983 to 1992, he was with the Institute of Nuclear Research, Pitesti, Romania, working on electronic instrumentation for nuclear power reactors. In 1993, he joined the Department of Electronics, University of Pitesti, Romania, as an Assistant Professor doing research in analogue circuits. From 1992 to 1993, he was a Fulbright Visiting Scholar at the Centre for Reliable Computing, Stanford University, Stanford, CA. In 1996, he joined Philsar Semiconductor, Ottawa, ON, Canada, as a Senior ASIC Designer, a company later acquired by Conexant Systems, Inc. (now known as Skyworks Solutions, Inc.). His work has been focused on the design of radio circuits for GPS receivers, Bluetooth transceivers, and GSM/CDMA cellular transceivers. He is presently a Technical Director with Skyworks Solutions Inc., Irvine, CA and is involved in designing circuits for Envelope Tracking and Front-End Modules in CMOS and SOI CMOS. He presented short courses and tutorials as an Invited Speaker at IEEE Microwave Theory and Techniques Society (MTT-S) International Microwave Symposium (IMS). European Microwave Week (EuMW), European Solid-State Circuits Conference (ESSCIRC) and Asia-Pacific Microwave Conference (APMC). He holds 98 U.S. patents, with several more pending. He is the author of the chapter "*Envelope Tracking Techniques*" in the IET book "*Radio Frequency and Microwave Power Amplifiers, Vol. 2: Efficiency and Linearity*".